Available online at www.sciencedirect.com
ScienceDirect
Trans. Nonferrous Met. Soc. China 35(2025) 1517−1531
Transactions of Nonferrous Metals Society of China
www.tnmsc.cn

Weakening of through-thickness texture gradient in tantalum plates by newly developed dynamic offsets and shear force adjustment rolling

Kai YU[1], Long-fei XU[1], Li WANG[1,2], Gui-peng LI[3], Xiao-dan ZHANG[4], Yu-hui WANG[1]

1. National Engineering Research Center for Equipment and Technology of Cold Strip Rolling, Yanshan University, Qinhuangdao 066004, China;
2. Faculty of Mechanical Engineering, Chongqing Industry Polytechnic College, Chongqing 401020, China;
3. Tongchuang Special Materials Co., Ltd., Lishui 323000, China;
4. Department of Civil and Mechanical Engineering, Technical University of Denmark, DK-2800 Kgs. Lyngby, Denmark

Received 27 September 2023; accepted 17 April 2024

Abstract: Traditional symmetrical rolling often induces through-thickness gradient microstructures and textures. In this study, ultra-high purity (99.999 wt.%) tantalum (Ta) served as a model material to address the texture gradient issue by employing dynamic offsets and shear force adjustment rolling (DS rolling) as an advanced rolling technique. The strain and stress distributions in Ta plates for DS rolling and symmetrical rolling processes were analyzed using Deform 3D software. Through-thickness textures and microstructures were characterized via electron backscatter diffraction. The results revealed that DS rolling effectively solved the problem of texture gradient by increasing the average shear strain from 0.05 to 0.56. In turn, the shear stress reduced the energy storage orientation dependence of {100} and {111} grains. Furthermore, DS rolling refined the recrystallized grains on an average of 30.9%.

Key words: tantalum; texture gradient; rolling; energy storage; shear stress

1 Introduction

Tantalum (Ta) is a rare metal characterized by high melting temperature (2996 °C) and excellent corrosion resistance, which allows it to be widely used in aerospace and medical fields [1−3]. With the rapid development of the semiconductor industry, Ta targets have found extensive applications in chip manufacturing. Ta is classified as a body-centered-cubic (BCC) metal with the high stacking fault energy (220 mJ/m^2) [4]. During conventional symmetrical rolling, Ta plates exhibit inhomogeneous microstructures and textures throughout their thickness direction [5]. Compared to the surface layers, rolled and annealed plates form a stronger {111}⟨*uvw*⟩ texture (γ-fiber) in the central layer [6]. The friction between rolls and plate surfaces induces a larger shear force on the surface layer than that experienced by the central layer, resulting in nearly zero shear stress within the latter layer [7]. Consequently, the Ta plate's center layer under compressive stress exhibits the γ-fiber texture [8], while the surface layer displays the {100}⟨*uvw*⟩ texture (θ-fiber) under compressive and shear stresses [9]. In general, {100} grains possess the relatively low stored energy and slow recrystallization speed [10], whereas {111} grains contain numerous micro-bands (MBs) and microshear bands (MSBs) with high-density dislocations [11]. As a result, recrystallization occurs faster in {111} grains than in {100} grains.

Corresponding author: Yu-hui WANG, Tel: +86-18630397227, E-mail: yhwang@ysu.edu.cn
https://doi.org/10.1016/S1003-6326(25)66764-1

Such orientation-dependent distribution of energy storage significantly impacts subsequent annealing processes since different driving forces may lead to texture aggregation and non-uniform grain size distribution [12,13]. In turn, the variations in grain size and orientation may severely impair the sputtering performance stability of Ta targets used in integrated circuits (ICs) [14].

Fortunately, severe plastic deformation (SPD) techniques, such as high-pressure torsion (HPT) and equal channel angular extrusion (ECAE) may effectively refine grains and homogenize their size distribution [15−18]. In this regard, HOSSEINI and KAZEMINEZHAD [19] significantly reduced the grain size and controlled the texture evolution of Ta through ECAE. WEI et al [20] achieved nanocrystalline Ta through high-strain-rate HPT. However, both processes are not applicable in industrial settings due to limited billet dimensions. Alternatively, asymmetrical rolling (ASR) may effectively address the challenges related to the through-thickness microstructure and texture inhomogeneity of Ta plates [10].

Uniform distributions of fine grains and textures have been enriched through shear deformation in SPD processes, such as ECAE, HPT, and ASR. Among these techniques, ECAE allows attaining shear angles ranging from 20° to 45° [21,22], while HPT can ensure shear angles up to 55° [23]. However, both methods are not suitable for large plate manufacturing. For comparison, ASR introduces shear deformation throughout the plate thickness under different roll speeds [24,25], with a limited shear angle range of 5°−15° [26,27].

Numerous studies have been conducted to investigate the impact of rolling parameters on the distribution of strain and stress [28−30]. For instance, SAGAPURAM et al [31] employed large strain extrusion machining (LSEM) to control the texture of magnesium alloy sheets. LIN et al [5] observed the improvement in microstructure homogeneity of ASRed Ta plates under a rolling velocity ratio (R_v) of 1.2 compared to that of 1.1.

In this work, Ta plates were produced by a newly developed dynamic offsets and shear force adjustment rolling (DS rolling) technique [32]. The DS rolling technique effectively reduced the plate curvature by adjusting the offset distance and speed ratio of working rolls. Additionally, the DS rolling shear angle was precisely controlled within the range of 0° to 45°. The DS rolling technology was shown to be potential for the widespread use in industrial production. A DS rolling rate R_v of 1.2 was selected to mitigate texture gradient throughout the thickness direction [33] while maintaining control over the geometry of roll gap (l/h, where l is the length of the contact between the rolls and specimen, and h refers to the average thickness of the sample for each rolling pass) in the deformation zone between 1.5 and 2.5 [34]. The influence of DS rolling shear force on the deformation microstructure and recrystallization behavior of Ta plates was investigated, and the results were discussed.

2 Experimental and simulation methods

2.1 Materials and procedures

Ultra-high purity tantalum ingots (99.999 wt.%) were produced via electron beam melting (EBM, Tongchuang Special Materials Co., Ltd.). The chemical composition of ingots is listed in Table 1. The 10 mm thick plates were afterward produced via multi-directional forging of Ta ingots, followed by heat treatment to refine coarse columnar crystals and rolling to ensure grain refinement.

Table 1 Chemical composition of Ta ingot specimens (10^{-6})

C	N	O	Nb	Mo	W
1	3	4	1	0.05	0.25

Ti	Si	Fe	Ni	Ta
<0.0005	<0.005	<0.005	<0.002	Balance

2.2 Rolling and annealing

The Ta plates underwent five processing passes to ensure a 70% reduction under the rolling parameters listed in Table 2, whereby the l/h ratio of the deformation zone's roll gap was controlled within the range of 1.5−2.5 [34]. The setup was designed by replacing the two-roller DS reversible cold rolling machine with bottom rolls of different diameters at the National Engineering Research Center for Equipment and Technology of Cold Strip Rolling, Yanshan University, China. The shear angle in the DS rolling experiments was set to be θ=35°. The respective deformation microstructures were studied by comparing symmetrical rolling and

Table 2 Processing parameters used in conventional rolling and DS rolling

Number of rolling pass	Entrance thickness, d_0/mm	Exit thickness, d/mm	Offset distance/m			Geometry of roll gap, l/h
			θ=20°	θ=35°	θ=45°	
1	10.0	7.2	3.36	5.04	7.20	1.50
2	7.2	5.4	2.52	3.78	5.40	1.65
3	5.4	4.2	1.96	2.94	4.20	1.76
4	4.2	3.5	1.63	2.45	3.50	1.68
5	3.5	3.0	1.40	2.10	3.00	1.69

$l/h=2\sqrt{R_{eq}(d_0-d)}/(d_0+d)$, where R_{eq} represents the equivalent radius of the rolling mill ($R_{eq}=2R_1R_2/(R_1+R_2)$; R_1 is the upper roll radius; R_2 is the bottom roll radius)

DS rolling. Subsequently, both groups of rolled specimens underwent low-temperature annealing under vacuum conditions at 500 °C for 10 min, followed by high-temperature annealing at 1000 °C for 10, 15, and 20 min to achieve fully recrystallized microstructures. Finally, the samples were cooled down to room temperature in the furnace.

Samples with dimensions of 10 mm × 2 mm × 3 mm were then sectioned from the initial specimens and exposed to wire cutting, rolling and annealing to obtain the plates. Samples used for microstructure and texture characterization were first mechanically polished and then electro-polished in a mixture of HF and H_2SO_4 with the volume ratio of 1∶9 at room temperature to remove any deformation and residual stress layers. The polishing consisted in maintaining the electric current at 0.1 A for 9 min until achieving surfaces with a metallic luster.

2.3 Materials characterization

The microstructures and local grain orientations in the ND−RD plane were examined via electron backscatter diffraction (EBSD, NordlysMax) integrated in a TESCAN MIRA 3 field emission gun scanning electron microscope. The measurements were conducted at an accelerating voltage of 20 kV and a working distance of 14 mm. The acquired data were post-processed using Channel 5 software. The Vickers hardness testing of the rolled plates was performed on a hardness tester (Qness Q10A) under a load of 200 g at a dwell time of 10 s. For each rolling condition, a total of 15 measurements were carried out on the RD−ND plane.

2.4 Model description

The models of symmetrical rolling, asymmetrical rolling, and DS rolling were established using Deform 3D software (Fig. 1). The deformation area in the symmetrical rolling with the rolls of the same diameter was divided into the front and back slip zones (Fig. 1(a)). For the asymmetrical rolling with a “Rub zone” between the front and back slip zones (Fig. 1(b)) [35], the bottom roll possessed a larger diameter than the upper roll, with a R_v value equal to 1.2 [36]. Based on the asymmetrical rolling in Fig. 1(c), DS rolling was achieved by offsetting the upper roll in the outlet direction. The schematic representation of the DS rolling deformation zone consisted of three parts: front slip zone I, rub zone II, and back slip zone III. During the multiple-pass rolling process, a constant shear angle was obtained by dynamically adjusting the offset distance. Furthermore, the effects of DS rolling shear angle on the plate curvature were investigated. The parameters of rolled plates and rolls are presented in Tables 3 and 4, respectively.

3 Results and discussion

3.1 Microstructures of initial tantalum plates

The inverse pole figure (IPF) map of a Ta plate before rolling is presented in Fig. 2(a). Fully recrystallized grains with near-equiaxed morphology and an average grain size of 99.8 μm were observed. Subsequent deformation through repeated upsetting and elongation of Ta ingots continuously refined the grain size to yield an equiaxed morphology [37]. The pole figure in Fig. 2(c) further demonstrated the Ta grains possessing a homogeneous orientation before rolling. The volume fractions of the {111}- and {100}-oriented grains accounted for 27.2% and 18.5%, respectively. However, the distribution of grain

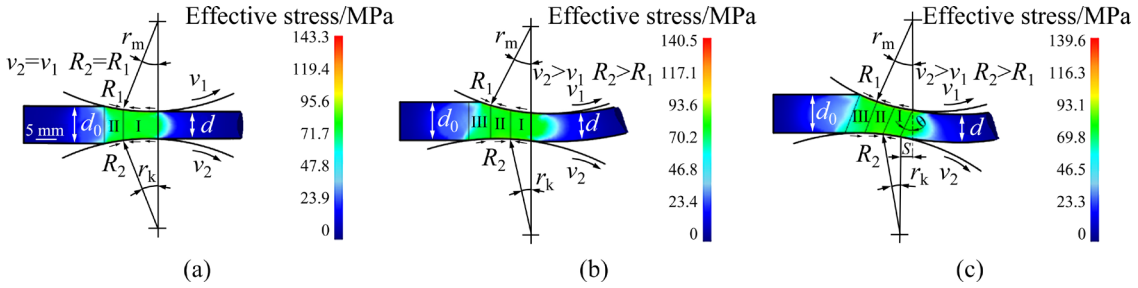

Fig. 1 Schematic diagrams of different rolling methods: (a) Symmetrical rolling; (b) Asymmetrical rolling; (c) DS rolling (v_1 and R_1 stand for the velocity and radius of the upper roll, respectively; v_2 and R_2 are the velocity and radius of the bottom roll, respectively; S is the horizontal offset distance; θ is the shear angle)

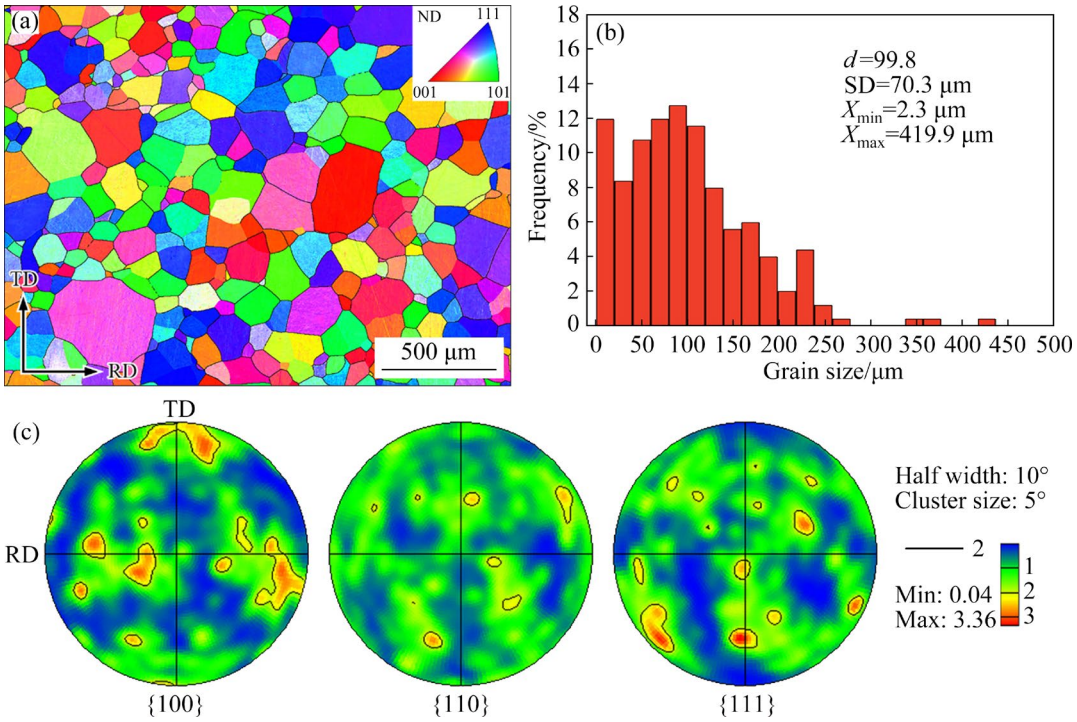

Fig. 2 Microstructure of Ta plates before rolling: (a) EBSD IPF map; (b) Corresponding grain size distribution; (c) Pole figures

Table 3 Initial conditions of material in rolling simulations

Material	Dimension/ mm	Environment temperature/°C	Heat transfer coefficient to environment/ ($W·m^{-2}·K^{-1}$)	Coulomb friction	Radiation coefficient
Ta	40×30×10	20	5	0.5	0.7

Table 4 Roll parameters used in conventional rolling and DS rolling

Upper roll diameter/mm	Bottom roll diameter/mm	Roll width/ mm	Rolling speed/ ($m·s^{-1}$)	Roll property
120	120/144	120	1−1.5	Rigid body

sizes appeared highly heterogeneous, with an average grain size (d) of 99.8 μm, a standard deviation (SD) as high as 70.3 μm and the largest grain size (X_{max}) measuring 419.9 μm.

3.2 DS rolling shear angle control and rolling procedures

The bending behavior of a plate can be quantified by its curvature (k) on the inner side,

which should be reciprocal to the curvature radius (R), meaning k=1/R. PHILIPP et al [38] and ANDERS et al [39] proposed that R can be calculated as the radius of a circumcircle formed by three selected points inside it. Accordingly, the coordinates (x_1, y_1), (x_2, y_2), and (x_3, y_3) were selected for the respective points 1, 2, and 3 in this study, while (x_c, y_c) represented the coordinate of the center of curvature. Thus, R can be determined by solving the equations below:

$$\begin{cases}(x_1-x_c)^2-(y_1-y_c)^2=R^2\\(x_2-x_c)^2-(y_2-y_c)^2=R^2\\(x_3-x_c)^2-(y_3-y_c)^2=R^2\end{cases} \quad (1)$$

A positive curvature was assigned for an upward plate bent, whereas a negative curvature indicated the downward bending. Figure 3 shows the impact of DS rolling shear angle on the plate curvature. The larger diameter of the asymmetrical bottom roll relative to that of the upper roll resulted in a higher metal flow rate beneath the surface layer than on the top. Consequently, the plate exhibited an upward bend with a curvature value of k=13.67 (Fig. 3(a)). The analysis of the parameters in Table 5 for asymmetrical and DS rolling processes revealed a shear angle of θ=35° inducing the flattest DS rolling plate profile with a minimal curvature (k=6.19). It is noteworthy that snake-like rolling enabled to control the plate profiles through offsetting distance and adjusting velocity ratios between rolls [40,41].

By contrast, DS rolling efficiently reduced the plate curvature by adjusting the shear angle. The upper roll was offset by a certain distance in the outlet direction, whereby a reverse bending force counteracted the plate bending forces. This subjected Ta plates to significant shear forces but also effectively calibrated their profiles while increasing deformation.

3.3 Microstructure after symmetrical and DS rolling

A self-designed two-roll DS reversible cold rolling machine is presented in Fig. 4(a). The profiles of Ta plates under different rolling processes are compared in Fig. 4(b). Similar to numerical simulation results, asymmetrical rolling resulted in smaller rolls and more pronounced bending. By contrast, DS rolling produced flatter and straighter plates. The hardness distributions along the ND for symmetrical and DS rolling samples are depicted in Fig. 5.

The bottom surface of the DS-rolled plates exhibited the higher hardness than the lower surface of symmetrical rolled plates, while the upper surfaces displayed similar hardness levels. This can be attributed to the larger bottom roll diameter and the greater deformation on the lower surface layer of each plate induced by DS rolling. On average, the DS-rolled samples exhibited a hardness of HV 173, being higher than that of the symmetrically

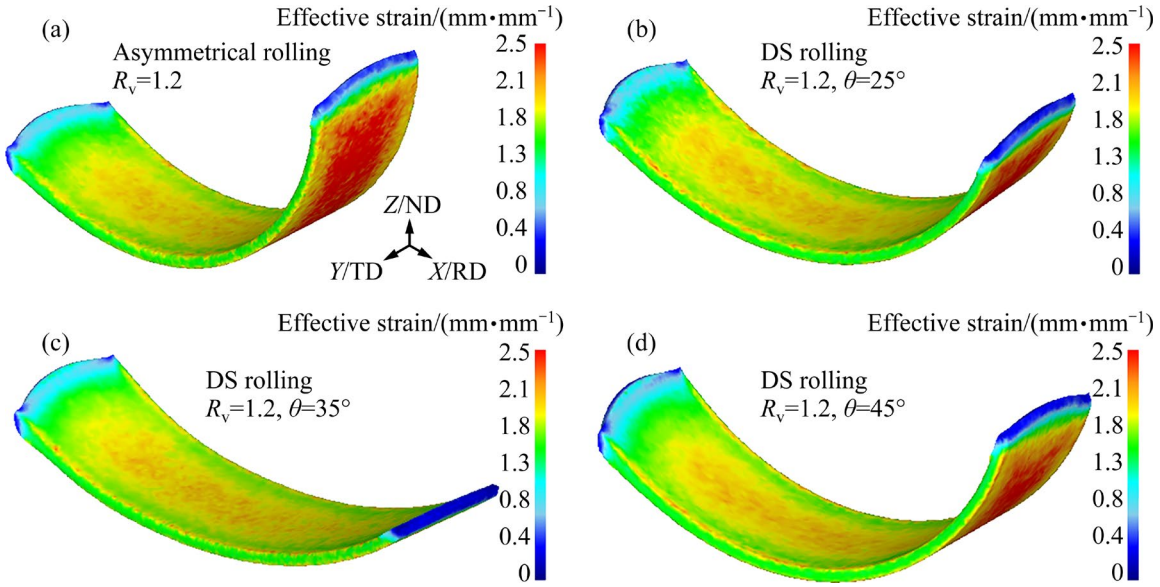

Fig. 3 Effect of shear angle on plate curvature: (a) Asymmetrical rolling; (b−d) DS rolling at θ=25°, θ=35° and θ=45°, respectively

Table 5 Comparison of plate curvature k between asymmetrical and DS rolling processes

Rolling process	Velocity ratio, R_v	Shear angle, θ/(°)	Curvature, k/m^{-1}
Asymmetrical rolling	1.2	15	13.67
DS rolling	1.2	25	12.24
DS rolling	1.2	35	6.19
DS rolling	1.2	45	13.97

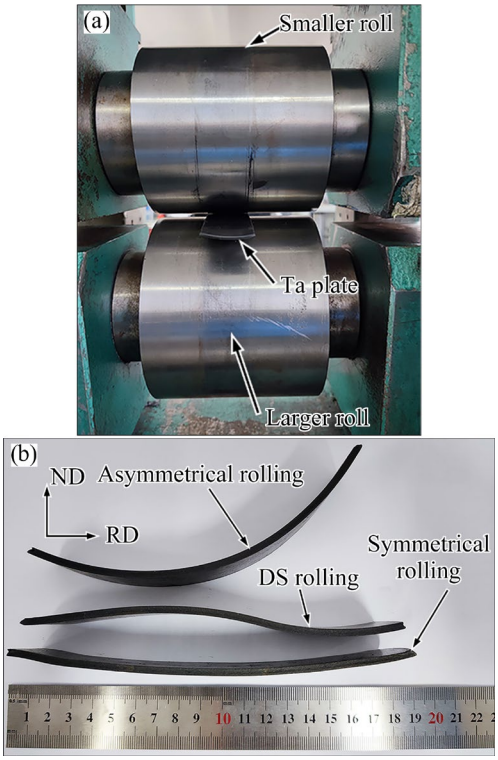

Fig. 4 Experimental equipment and rolled Ta plates: (a) Two-roll DS reversible cold rolling machine; (b) Plate profile comparison between different rolling processes

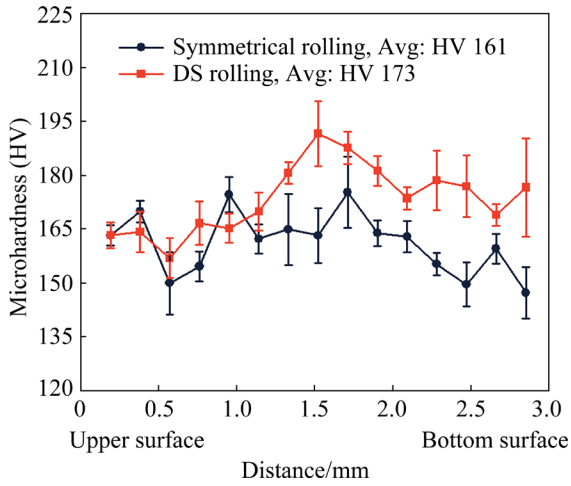

Fig. 5 Microhardness of Ta plates after symmetrical rolling and DS rolling

rolled specimens (HV 161). Therefore, the deformation in the DS-rolled samples exceeded that in symmetrically rolled specimens.

The EBSD IPF maps in Fig. 6 identified the presence of {100} and {110} grain orientations in the near-surface region of symmetrically rolled Ta plates, covering the area of approximately 3 mm^2. In the central layer of the plate, a significant texture gradient was observed with multiple {111}-oriented grains, indicating their formation (Fig. 6(a)). Consequently, DS rolling samples exhibited the alternating and homogeneous distribution patterns along the ND for both deformed grains with {111} and {100} orientations (Fig. 6(b)).

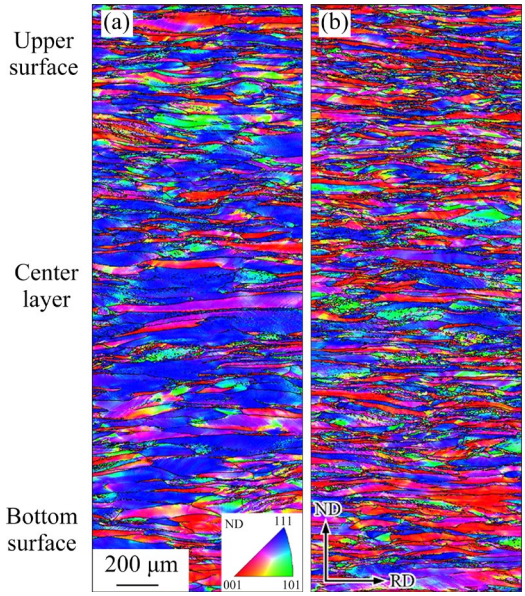

Fig. 6 Large area EBSD IPF maps of deformation microstructure along thickness direction of specimens after 70% rolling reduction: (a) Symmetrical rolling; (b) DS rolling

Cold-rolled Ta plates with body-centered cubic (BCC) structure were primarily composed of α-fiber (⟨110⟩//RD), γ-fiber (⟨111⟩//ND), and θ-fiber (⟨100⟩//ND) structures [42]. The three fibers can be visualized within the Euler space on a section of ϕ_2=45° [43]. After the thickness reduction by 70%, symmetrical rolling specimens displayed a dominant γ-fiber texture with a maximum intensity of approximately 6.5. By comparison, DS rolling samples exhibited the mixed θ-fiber and γ-fiber textures from the ODF maps with a relatively small maximum intensity between them (about 3.38 in Fig. 7). Furthermore, DS rolling reduced the γ-fiber content from 52.3% to 35.7% while increasing the θ-fiber content from 16.8% to 20.2%, which

resulted in more homogenous grain orientation distributions (Fig. 7(d)).

The grain deformation behavior was further analyzed by extracting the smaller scan regions from the large-area EBSD maps (Fig. 8). As depicted in Fig. 8(d), the DS rolling specimens exhibited a significantly finer deformation microstructure than the symmetrical rolling samples. Similarly, ZHOU et al [44] observed {111} grains containing fine subgrains in DPD-processed samples. In the conventional symmetrical rolling, notable disparities in grain boundary distributions

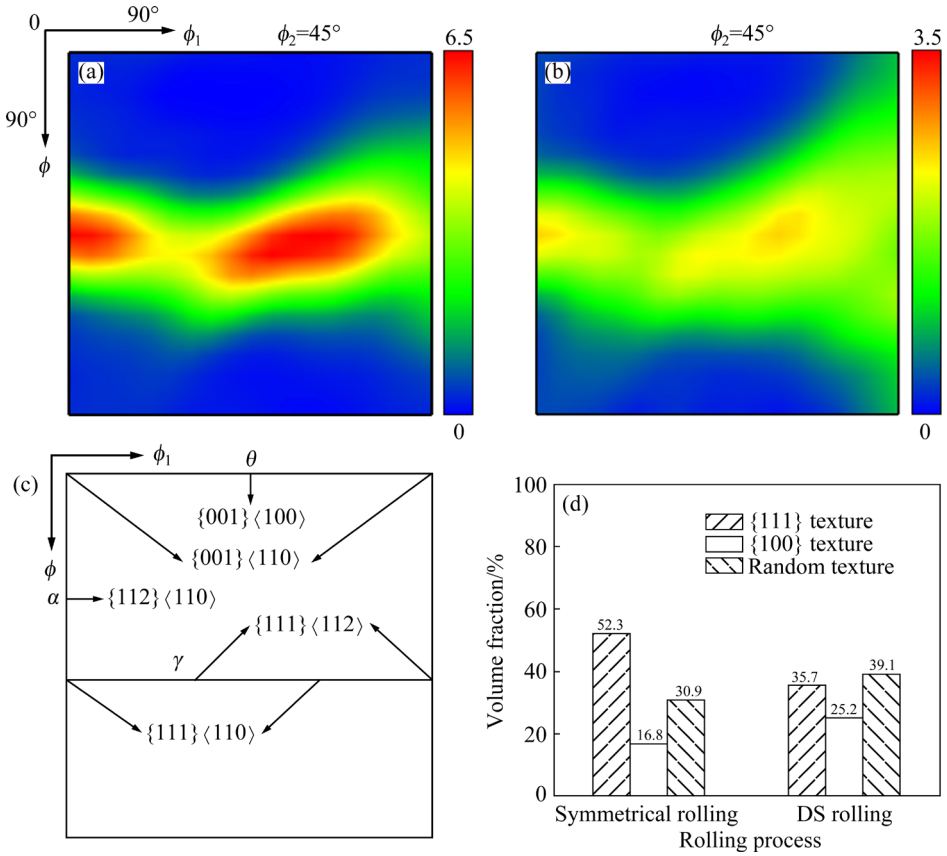

Fig. 7 Orientation distribution function (ODF) sections in specimens after symmetrical rolling (a) and DS rolling (b) with orientation relationship plot (c) and quantitative texture contents obtained by symmetrical rolling and DS rolling (d)

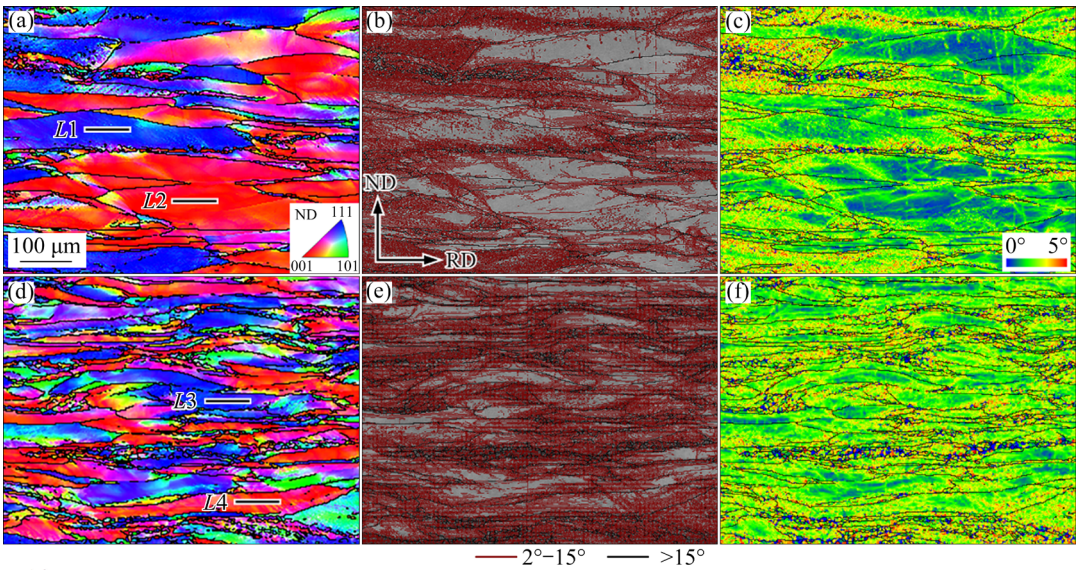

Fig. 8 Inverse pole figure (IPF) (a, d), grain boundary distribution (b, e), and kernel average misorientation (KAM) (c, f) maps of symmetrically rolled (a−c) and DS rolled (d−f) samples

were observed in deformed {100} and {111} grains (Figs. 8(a) and (b)). In the image, the dark and maroon solid lines represent the high-angle (>15°) and low-angle (2°−15°) grain boundaries, respectively. The {111} grains contained numerous low-angle grain boundaries, while the {100} grains displayed only a few low-angle grain boundaries.

Conversely, the grain boundaries in DS-rolled samples were uniformly distributed. Therefore, the specimens subjected to symmetrical rolling exhibited a strong orientation dependence on the local energy storage [45], which was evaluated from the spacing and misorientation across the low-angle grain boundaries [46,47]. Additionally, the KAM values of deformed {111} grains exceeded those of {100} grains (Fig. 8(c)). Similar trends were also observed in the DS-rolled specimen (Figs. 8(d−f)). However, the DS rolling led to a much higher shear strain throughout the specimen thickness, reducing the spacing between the high-angle grain boundaries from 60.6 μm for the symmetrical rolling to 23.4 μm for the DS rolling. It is noteworthy that the high-angle grain boundary spacing size was measured via the interception method, which reflected the higher-degree grain subdivisions under higher deformation strains [48−50]. As a result, the average value (E_x) of point-to-point misorientations within the {100} grains increased from 0.45° for the symmetrical rolling (Fig. 9(a)) to 1.55° for the DS rolling (Fig. 9(b)). In turn, such enhancement weakened the crystallographic orientation dependence of the deformation-induced stored energy difference between {111} and {100} texture components. Additionally, a more uniform distribution of KAM values in DS-rolled samples was observed in Fig. 8(f). Hence, DS rolling promoted a more random energy storage distribution within the grains, as well as improved the deformation microstructure uniformity in Ta plates.

3.4 Comparison of shear strain and stress distribution between symmetrical rolling and DS rolling

Compared to the centerline, the upper and bottom parts of the rolling plate underwent asymmetrical deformations during DS rolling, resulting in different shear stress distributions on their respective contact surfaces. Figure 10 represents the shear stress distribution within both

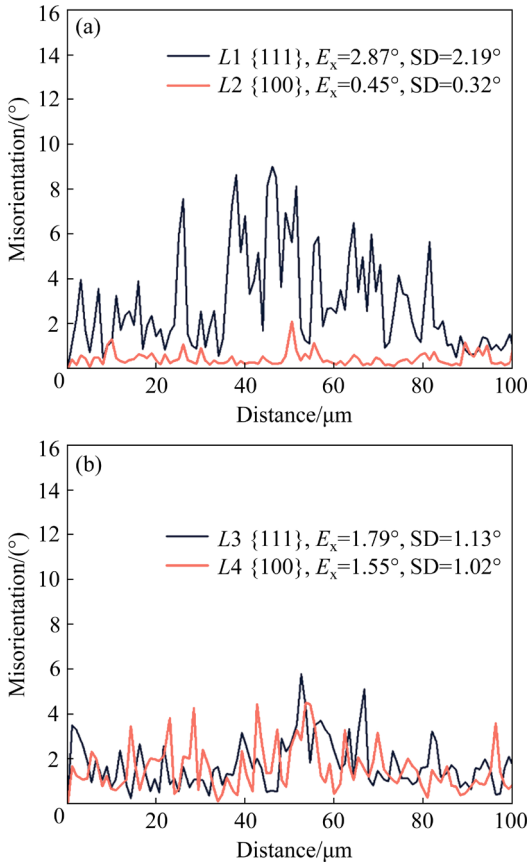

Fig. 9 Point-to-point misorientation angle distribution along lines $L1$−$L4$ in Fig. 8: (a) Symmetrical rolling; (b) DS rolling

DS and symmetrically rolled plates. Obviously, symmetrically rolled plates exhibited a symmetric shear stress distribution at their contact points on both the upper and bottom surfaces (Fig. 10(a)). However, a “rub zone” was formed between the front and back slide zones during DS rolling (Fig. 10(b)). Within this region, complex negative shear stresses were observed due to anti-directional friction forces acting on both roll surfaces, resulting in the vertical compressive strain and the horizontal shear strain on the plate, which caused the greater deformation when compared to symmetrical rolling.

The shear strain distributions in symmetrically rolled and DS-rolled specimens after a 70% reduction are compared in Fig. 11. The comparison of Figs. 11(a) and (b) revealed that DS rolling induced the larger shear strain than symmetrical rolling owing to the faster metal flow on the bottom surface. In Fig. 11(c), the thickness of the rolled plate was divided into 13 units (numbered from top to bottom as 1 to 13). The first and thirteenth units represented respectively the uppermost and lowermost layers of

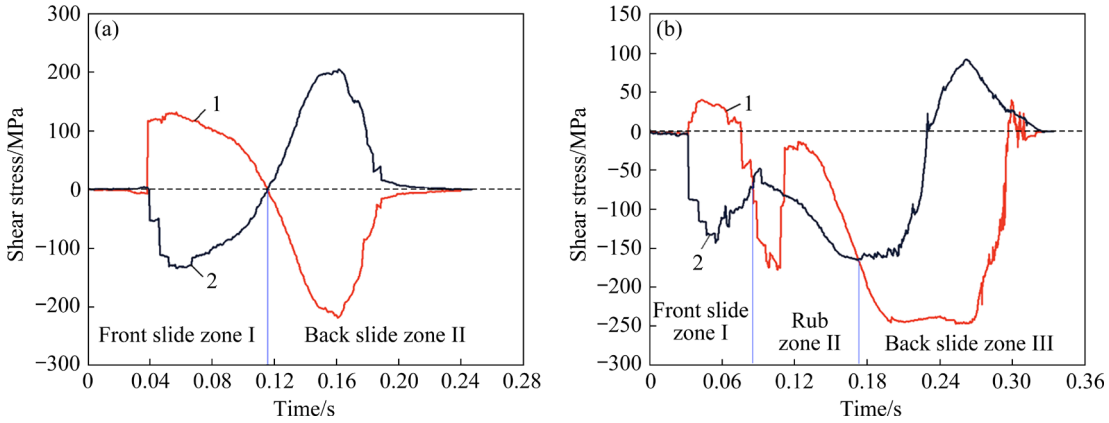

Fig. 10 Distributions of shear stress in deformation zone: (a) Symmetrical rolling; (b) DS rolling (1: Contact point between upper roll and plate; 2: Contact point between bottom roll and plate)

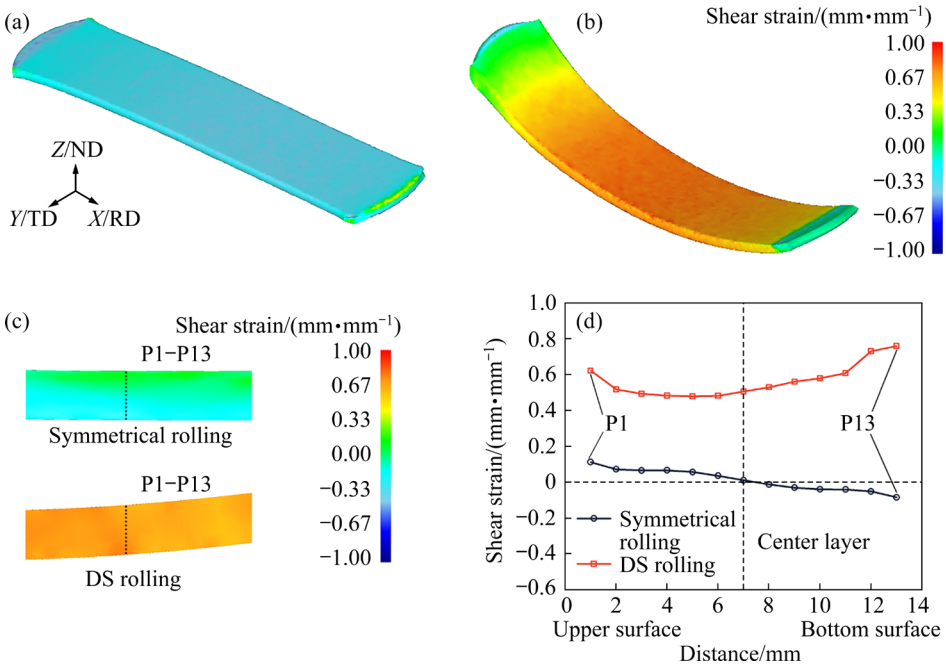

Fig. 11 Shear strain distributions of shear strain: (a) Symmetrical rolling; (b) DS rolling; (c) Comparison of shear strain on sections of rolled plates (70% reduction); (d) Shear strain distributions along plate thickness direction for symmetrical rolling and DS rolling

the plate, while the seventh unit showed its central layer. In Fig. 11(c), an almost zero shear strain was recorded along the ND direction during symmetrical rolling. The upper half of the plate demonstrated a positive shear strain, while the bottom half displayed a negative shear strain.

By contrast, the shear strain was positive in the thickness direction of DS-rolled plates. As for the distribution of the shear strain component (ε_{XZ}) at the end of each unit (Fig. 11(d)), symmetrical rolling resulted in nearly zero shear strain, while DS rolling induced significant shear strain in the plate thickness direction. The average shear strain ε_{XZ} increased from 0.05 to 0.56, indicating the increase in shear strain penetration depth into the central region of the plate through DS rolling as a function of velocity ratio and “reverse bending force”. Moreover, symmetrical rolling generated surface shear strain due to the roll friction, whereas DS rolling promoted severe shear strain in the “rub zone”. Under the normal stress conditions, the {100} grains displayed high stability but were prone to deformation under shear stress [5]. In the conventional symmetrical rolling, a minimal or zero shear stress occurred within the center layer when compared to that on the surface layer (Fig. 11(c)).

This resulted in a texture gradient emerging from the rolled surface toward the center during symmetrical rolling of Ta plates. The shear strain was negligible in this central layer (Fig. 11(d)), which was consistent with numerical simulation results, leading to the formation of an extremely strong γ-fiber texture. On the other hand, roll friction generated shear stress on the surface layer of the symmetrically rolled plate, leading to the formation of the θ-fiber texture. By contrast, DS rolling effectively addressed the problem of texture gradient by introducing the high shear stress throughout the thickness direction of Ta plates (Fig. 11(d)). The above numerical simulation data were subsequently validated by experimental investigations.

3.5 Effect of shear stress on recrystallization microstructure

Microstructures of 70%-reduced symmetrically rolled and DS-rolled samples under the same pre-recovery treatment conditions (500 °C for 10 min) followed by high-temperature annealing at different parameters (1000 °C for 10, 15, and 20 min) are displayed in Fig. 12. The sub-grains formed during the low-temperature pre-recovery exhibited the equiaxial microstructural morphology [43]. SRINIVASAN et al [51] also observed a decrease in hardness difference between {111}- and {100}-oriented niobium single crystals from 40% before recovery to 20% after recovery. Consequently, all samples were subjected to low-temperature annealing at 500 °C for 10 min. As shown in Figs. 12(a)

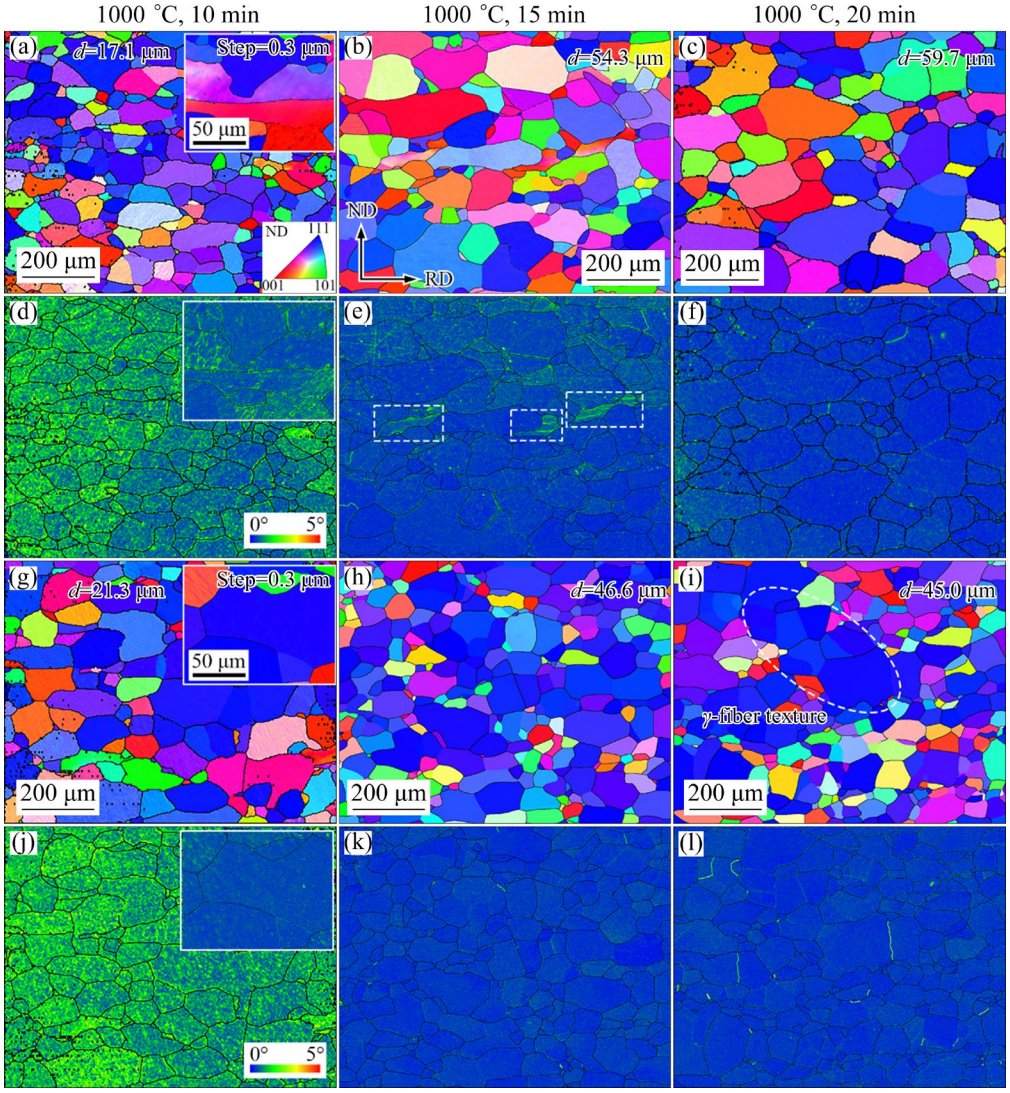

Fig. 12 Symmetrically rolled and DS-rolled samples subjected to same pre-recovery annealing conditions (500 °C for 10 min) followed by high-temperature annealing at 1000 °C for 10, 15, and 20 min: (a−c) IPF maps of symmetrically rolled samples; (d−f) KAM maps corresponding to (a−c), respectively; (g−i) IPF maps of DS rolling samples; (j−l) KAM maps corresponding to (g−i), respectively

and (g), samples subjected to high-temperature annealing at 1000 °C for 10 min yielded the complete recrystallization. However, dislocations were observed within some grains. In Figs. 12(d) and (j), the KAM maps indicated the presence of low-angle grain boundaries. The previous research [52] suggested a proportional relationship between dislocation density and local misorientation. As displayed in the upper right corner of Fig. 12(d), significant differences in KAM values between {111} and {100} grains were observed in the symmetrically rolled sample. Conversely, the KAM values were more uniformly distributed in the DS-rolled sample (see the upper right corner of Fig. 12(j)), significantly reducing the dislocation density among differently oriented grains, including {111} and {100} ones. Once the annealing duration rose to 15 min at 1000 °C, some deformation structures remained in the symmetrically rolled sample (highlighted with frames in Fig. 12(e)).

For comparison, the annealed microstructure of DS-rolled samples exhibited a fully recrystallized state, characterized by grains with relatively random orientations and an average size of up to 46.6 μm. At the same 70%-reduced thickness, DS-rolled samples displayed severer deformation, indicating the higher dislocation density and faster grain growth rate. The extension of the annealing time for equiaxed crystals in the symmetrically rolled sample resulted in an average grain size of 59.7 μm and the absence of dislocations in the grains (Figs. 12(c) and (f)). The shear stress during DS rolling reduced the annealing time from 20 to 15 min. However, a further growth of {111} grains formed a stronger γ-fiber texture (see ellipse in Fig. 12(i)). This can be explained by the high-angle grain boundary migration nucleation mechanism driven by the high storage energy of {111} grains, which rapidly engulfed the deformation structure to ensure the formation of new grains [53]. The dislocation density within {100} grains was lower at nucleation points located only at grain boundaries. Moreover, the insufficient driving force provided by the deformation structure eliminated the smaller {100} recrystallized grains lacking a significant growth potential. The longer annealing time for Ta plates resulted in higher proportions of γ-fiber texture.

Fully recrystallized microstructures were achieved by subjecting the DS-rolled samples to annealing at 1000 °C for 15 min. By comparison, the symmetrically rolled samples required an annealing time of 20 min to achieve complete recrystallization. The large-area EBSD maps (approximately 3 mm^2 in Fig. 13) revealed the fine grains with the average size of 44.1 μm in a DS-

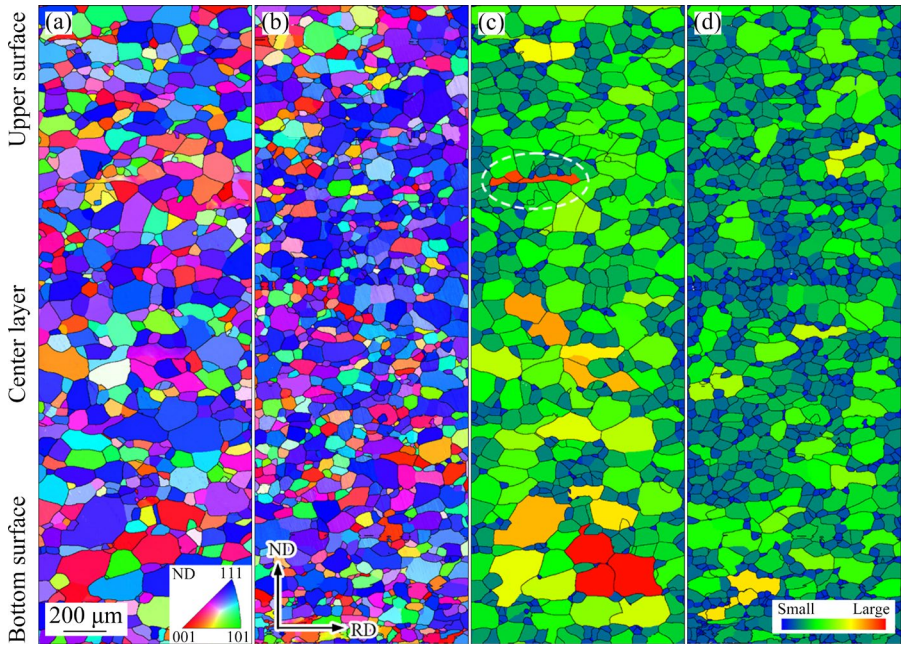

Fig. 13 Large-area EBSD maps of completely recrystallized microstructures: (a) Symmetrically rolled sample subjected to pre-recovery annealing at 500 °C for 10 min, followed by high-temperature annealing at 1000 °C for 20 min; (b) DS-rolled sample subjected to annealing at 500 °C for 10 min, followed by high-temperature annealing at 1000 °C for 15 min; (c, d) Grain size distribution maps corresponding to (a) and (b), respectively

rolled sample after annealing. In Figs. 13(c) and (d), the DS-rolled sample (SD=30.4 μm) exposed to annealing exhibited a homogeneously distributed grain size. Conversely, the symmetrically rolled sample after annealing displayed a relatively uneven grain size (SD=47.9 μm), including abnormally large grains with an average grain size of approximately 63.8 μm. As indicated by the ellipse in Fig. 13(c), the presence of deformation bands and the non-uniform microstructure distribution may significantly affect the properties of Ta sputtering targets [14]. Moreover, the DS rolling induced shear stress refined the grains by approximately 30.9% (Figs. 14(a) and (b)). Furthermore, the DS-rolled sample with a fairly uniform grain size distribution was more advantageous for ensuring stability during Ta target sputtering.

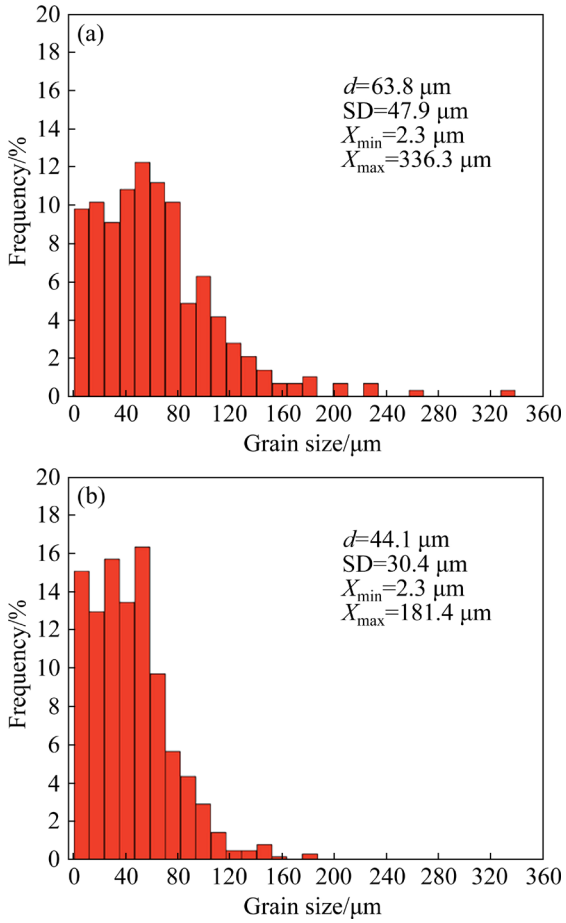

Fig. 14 Grain size histograms of symmetrically rolled (a) and DS-rolled (b) samples

4 Conclusions

(1) The numerical simulation indicated that DS rolling introduced shear stress into the central layer of the plates, increasing shear strain from 0.05 to 0.56 when compared to symmetrical rolling.

(2) The DS rolling significantly improved the texture homogeneity of Ta plates across the thickness, which was attributed to the formation of a strong γ-fiber texture under compressive stress, while θ-fiber and γ-fiber textures were formed under combined compressive and shear stresses.

(3) The shear stress effectively reduced the energy storage orientation dependence of {100} and {111} grains, thereby significantly enhancing the homogeneity of through-thickness grain size distribution in annealed samples. Additionally, DS rolling accelerated recrystallization and resulted in a 30.9% reduction in grain size relative to symmetrical rolling.

CRediT authorship contribution statement

Kai YU: Conceptualization, Methodology, Investigation, Writing – Original draft, Review & editing; **Long-fei XU:** Methodology, Validation, Investigation, Writing – Review & editing; **Li WANG:** Methodology, Validation, Investigation; **Gui-peng LI:** Resources, Investigation, Writing – Review & editing; **Xiao-dan ZHANG:** Writing – Review & editing; **Yu-hui WANG:** Conceptualization, Funding acquisition, Resources, Writing – Original draft, Review & editing.

Declaration of competing interest

The authors declare that they have no known competing financial interests or personal relationships that could have appeared to influence the work reported in this paper.

Acknowledgments

The research was funded by the National Key Research and Development Program of China (No. 2022YFB3705504), the Key Research and Development Program of Hebei Province, China (No. 21310301D), the Central Government Guidance Fund for Local Science and Technology, China (No. 226Z1003G), and the Natural Science Foundation Innovation Group Funding Project of Hebei Province, China (No. E2021203011).

References

[1] LO C L, CATALANO M, KHOSRAVI A, GE W Y, JI Y J, ZEMLYANOV D Y, WANG L H, ADDOU R, LIU Y Y,

WALLACE R M, KIM M J, CHEN Z H. Enhancing interconnect reliability and performance by converting tantalum to 2D layered tantalum sulfide at low temperature [J]. Advanced Materials, 2019, 31(30): 1902397.

[2] GAO Hai-rui, YANG Jing-zhou, JIN Xia, QU Xin-hua, ZHANG Fa-qiang, ZHANG Da-chen, CHEN Hai-shen, WEI Hui-ling, ZHANG Sui-pei, JIA Wei-tao, YUE Bing, LI Xiao-peng. Porous tantalum scaffolds: Fabrication, structure, properties, and orthopedic applications [J]. Materials & Design, 2021, 210: 110095.

[3] XU Jia-wei, XIAO Lai-rong, ZHANG Ya-fang, DENG Guan-zhi, LIU Guan-qun, WU Rui-lin, SHEN Hong-tai, ZHAO Xiao-jun, LIU Sai-nan, CAI Zhen-yang. Ultra-high temperature oxidation resistance of a $MoSi_2$ composite coating with TaB_2 diffusion barrier on tantalum alloy [J]. Corrosion Science, 2023, 224: 111563.

[4] OSTAFIN M, POSPIECH J, SCHWARZER R A. Microstructure and texture in copper sheets after reverse and cross rolling [J]. Solid State Phenomena, 2005, 105: 309−314.

[5] LIN Nan, LIU Shi-feng, LIU Ya-hui, FAN Hai-yang, ZHU Jia-lin, DENG Chao, LIU Qing. Effects of asymmetrical rolling on through-thickness microstructure and texture of body-centered cubic (BCC) tantalum [J]. International Journal of Refractory Metals and Hard Materials, 2019, 78: 51−60.

[6] ZHU Jia-lin, LIU Shi-feng, YUAN Xiao-li, LIU Qing. Comparing the through-thickness gradient of the deformed and recrystallized microstructure in tantalum with unidirectional and clock rolling [J]. Materials (Basel), 2019, 12(1): E169.

[7] ZHANG Tao, WU Yun-xin, GONG Hai, ZHENG Xi-zhao, JIANG Shao-song. Effects of rolling parameters of snake hot rolling on strain distribution of aluminum alloy 7075 [J]. Transactions of Nonferrous Metals Society of China, 2014, 24(7): 2150−2156.

[8] BATON J, GESLIN W, MOUSSA C. Orientation and deformation conditions dependence of dislocation substructures in cold deformed pure tantalum [J]. Materials Characterization, 2021, 171: 110789.

[9] BATON J, GESLIN W, MOUSSA C. Influence of crystallographic orientation on the recrystallization of pure tantalum through microstructure-based estimation of the stored energy [J]. International Journal of Refractory Metals and Hard Materials, 2022, 104: 105786.

[10] ZHU Jia-lin, LIU Shi-feng, LONG Dou-dou, LIU Ya-hui, LIN Nan, YUAN Xiao-li, ORLOV D. Asymmetric cross rolling: A new technique for alleviating orientation-dependent microstructure inhomogeneity in tantalum sheets [J]. Journal of Materials Research and Technology, 2020, 9(3): 4566−4577.

[11] LIU Y H, LIU S F, ZHU J L, DENG C, FAN H Y, CAO L F, LIU Q. Strain path dependence of microstructure and annealing behavior in high purity tantalum [J]. Materials Science and Engineering: A, 2017, 707: 518−530.

[12] DENG C, LIU S F, FAN H Y, HAO X B, JI J L, ZHANG Z Q, LIU Q. Elimination of elongated bands by clock rolling in high-purity tantalum [J]. Metallurgical and Materials Transactions A, 2015, 46: 5477−5481.

[13] DEY S, GAYATHRI N, BHATTACHARYA M, MUKHERJEE P. In situ XRD studies of the process dynamics during annealing in cold-rolled copper [J]. Metallurgical and Materials Transactions A, 2016, 47: 6281−6291.

[14] MICHALUK C A. Correlating discrete orientation and grain size to the sputter deposition properties of tantalum [J]. Journal of Electronic Materials, 2002, 31: 2−9.

[15] BEAUSIR B, SUWAS S, TÓTH L S, NEALE K W, FUNDENBERGER J J. Analysis of texture evolution in magnesium during equal channel angular extrusion [J]. Acta Materialia, 2008, 56(2): 200−214.

[16] AGNEW S R, MEHROTRA P, LILLO T M, STOICA G M, LIAW P K. Crystallographic texture evolution of three wrought magnesium alloys during equal channel angular extrusion [J]. Materials Science and Engineering: A, 2005, 408(1/2): 72−78.

[17] ZHANG Y S, WEI Q M, NIU H Z, LI Y S, CHEN C, YU Z T, BAI X F, ZHANG P X. Formation of nanocrystalline structure in tantalum by sliding friction treatment [J]. International Journal of Refractory Metals and Hard Materials, 2014, 45: 71−75.

[18] CHAE J M, LEE K O, AMANOV A. Gradient nanostructured tantalum by thermal-mechanical ultrasonic impact energy [J]. Materials (Basel), 2018, 11(3): E452.

[19] HOSSEINI E, KAZEMINEZHAD M. Dislocation structure and strength evolution of heavily deformed tantalum [J]. International Journal of Refractory Metals and Hard Materials, 2009, 27(3): 605−610.

[20] WEI Q, PAN Z L, WU X L, SCHUSTER B E, KECSKES L J, VALIEV R Z. Microstructure and mechanical properties at different length scales and strain rates of nanocrystalline tantalum produced by high-pressure torsion [J]. Acta Materialia, 2011, 59(6): 2423−2436.

[21] MUKAI T, YAMANOI M, WATANABE H, HIGASHI K. Ductility enhancement in AZ31 magnesium alloy by controlling its grain structure [J]. Scripta Materialia, 2001, 45(1): 89−94.

[22] AGNEW S R, HORTON J A, LILLO T M, BROWN D W. Enhanced ductility in strongly textured magnesium produced by equal channel angular processing [J]. Scripta Materialia, 2004, 50(3): 377−381.

[23] YUAN W, MISHRA R S. Grain size and texture effects on deformation behavior of AZ31 magnesium alloy [J]. Materials Science and Engineering: A, 2012, 558: 716−724.

[24] ZHANG Wen-cong, LIU Xin-tong, MA Jun-fei, WANG Wen-ke, CHEN Wen-zhen, LIU Yu-xuan, YANG Jian-lei. Evolution of microstructure and mechanical properties of ZK60 magnesium alloy processed by asymmetric lowered-temperature rolling [J]. Transactions of Nonferrous Metals Society of China, 2022, 32(9): 2877−2888.

[25] UNIWERSAŁ A, WROŃSKI M, WRÓBEL M, WIERZBANOWSKI K, BACZMAŃSKI A. Texture effects due to asymmetric rolling of polycrystalline copper [J]. Acta Materialia, 2017, 139: 30−38.

[26] STANFORD N, BARNETT M. Effect of composition on the texture and deformation behaviour of wrought Mg alloys [J].

Scripta Materialia, 2008, 58(3): 179−182.

[27] HUANG X S, SUZUKI K, SAITO N. Textures and stretch formability of Mg−6Al−1Zn magnesium alloy sheets rolled at high temperatures up to 793 K [J]. Scripta Materialia, 2009, 60(8): 651−654.

[28] ZUO Fang-qing, JIANG Jian-hua, SHAN Ai-dang, FANG Jian-min, ZHANG Xing-yao. Shear deformation and grain refinement in pure Al by asymmetric rolling [J]. Transactions of Nonferrous Metals Society of China, 2008, 18(4): 774−777.

[29] MOUSAVI S A A A, EBRAHIMI S M, MADOLIAT R. Three dimensional numerical analyses of asymmetric rolling [J]. Journal of Materials Processing Technology, 2007, 187: 725−729.

[30] DING H L, KANAMORI N, HONMA T, KAMADO S, KOJIMA Y. FEM analysis for hot rolling process of AM60 alloy [J]. Transactions of Nonferrous Metals Society of China, 2008, 18: s242−s246.

[31] SAGAPURAM D, EFE M, MOSCOSO W, CHAND-RASEKAR S, TRUMBLE K P. Controlling texture in magnesium alloy sheet by shear-based deformation processing [J]. Acta Materialia, 2013, 61(18): 6843−6856.

[32] WANG Yu-hui, XU Long-fei, ZHENG Ya-nan, KONG Ling, QI Xiang-dong, PENG Yan. Rolling process of complete set of DS rolling mill equipment and its control plate shape: China Patent, CN114932147B [P]. 2023−02−28.

[33] LONG Dou-dou, LIU Shi-feng, ZHU Jia-lin, LIU Ya-hui, ZHOU Shi-yuan, YUAN Xiao-li, ORLOV D. Improving texture and microstructure homogeneity in high-purity Ta sheets by warm cross rolling and annealing [J]. Metals, 2021, 11(11): 1665.

[34] ZHU Jia-lin, LIU Shi-feng, LONG Dou-dou, ORLOV D, LIU Qing. Pass number dependence of through-thickness microstructure homogeneity in tantalum sheets under the change of strain path [J]. Materials Characterization, 2020, 160: 110076.

[35] QWAMIZADEH M, KADKHODAEI M, SALIMI M. Asymmetrical sheet rolling analysis and evaluation of developed curvature [J]. The International Journal of Advanced Manufacturing Technology, 2012, 61: 227−235.

[36] WANG Ji, LIU Xiang-hua, SUN Xiang-kun. Study on the relationship between asymmetrical rolling deformation zone configuration and rolling parameters [J]. International Journal of Mechanical Sciences, 2020, 187: 105905.

[37] CLARK JR J B, GARRETT JR R K, JUNGLING T L, ASFAHANI R I. Influence of initial ingot breakdown on the microstructural and textural development of high-purity tantalum [J]. Metallurgical Transactions A, 1991, 22(12): 2959−2968.

[38] PHILIPP M, SCHWENZFEIER W, FISCHER F D, WÖDLINGER R, FISCHER C. Front end bending in plate rolling influenced by circumferential speed mismatch and geometry [J]. Journal of Materials Processing Technology, 2007, 184(1/2/3): 224−232.

[39] ANDERS D, MÜNKER T, ARTEL J, WEINBERG K. A dimensional analysis of front-end bending in plate rolling applications [J]. Journal of Materials Processing Technology, 2012, 212(6): 1387−1398.

[40] YANG Ji-xiang, LI Sai-yi, LIU Jie, LI Xue-wen, ZHANG Xin-ming. Finite element analysis of bending behavior and strain heterogeneity in snake rolling of AA7050 plates using a hyperbolic sine-type constitutive law [J]. Journal of Materials Processing Technology, 2017, 240: 274−283.

[41] LI Sai-yi, QIN Nan, LIU Jie, ZHANG Xin-ming. Microstructure, texture and mechanical properties of AA1060 aluminum plate processed by snake rolling [J]. Materials & Design, 2016, 90: 1010−1017.

[42] RAABE D. Simulation of rolling textures of bcc metals considering grain interactions and crystallographic slip on {110}, {112} and {123} planes [J]. Materials Science and Engineering: A, 1995, 197(1): 31−37.

[43] LIU S F, LIU Y H, LI L J, DENG C, FAN H Y, GUO Y, CAO L F, LIU Q. Effects of pre-recovery on the recrystallization microstructure and texture of high-purity tantalum [J]. Journal of Materials Science, 2018, 53: 2985−2994.

[44] ZHOU Shi-yuan, LIU Shi-feng, ZHAO Hang, DENG Chao, LIU Ya-hui, ZHANG Zhi-qing, YUAN Xiao-li. Effects of initial textures on the microstructure and annealing behavior of tantalum after dynamic plastic deformation [J]. Materials Characterization, 2022, 192: 112247.

[45] DENG C, LIU S F, HAO X B, JI J L, ZHANG Z Q, LIU Q. Orientation dependence of stored energy release and microstructure evolution in cold rolled tantalum [J]. International Journal of Refractory Metals and Hard Materials, 2014, 46: 24−29.

[46] PAN Hong-jiang, HE Yue, ZHANG Xiao-dan. Interactions between dislocations and boundaries during deformation [J]. Materials, 2021, 14(4): 1012.

[47] YAN Ying-rui, PAN Hong-jiang, GODFREY A, JENSEN D J, ZHANG Xiao-dan. Stored energy calculation in AA 1050 based on deformation microstructure from electron backscatter diffraction data [J]. IOP Conference Series: Materials Science and Engineering, 2022, 1249(1): 012064.

[48] ZHANG Xiao-dan, HANSEN N, GAO Yu-kui, HUANG Xiao-xu. Hall–Petch and dislocation strengthening in graded nanostructured steel [J]. Acta Materialia, 2012, 60(16): 5933−5943.

[49] ZHANG Xiao-dan, NIELSEN C V, HANSEN N, SILVA C M, MARTINS P A. Local stress and strain in heterogeneously deformed aluminum: A comparison analysis by microhardness, electron microscopy and finite element modelling [J]. International Journal of Plasticity, 2019, 115: 93−110.

[50] ZHANG X, HANSEN N, NIELSEN C V. Local microstructure and flow stress in deformed metals [J]. IOP Conference Series: Materials Science and Engineering, 2017, 219(1): 012053.

[51] SRINIVASAN R, VISWANATHAN G B, LEVIT V I, FRASER H L. Orientation effect on recovery and recrystallization of cold rolled niobium single crystals [J]. Materials Science and Engineering: A, 2009, 507(1/2): 179−189.

[52] ATEBA BETANDA Y, HELBERT A L, BRISSET F, MATHON M H, WAECKERLÉ T, BAUDIN T. Measurement of stored energy in Fe−48%Ni alloys strongly

cold-rolled using three approaches: Neutron diffraction, Dillamore and KAM approaches [J]. Materials Science and Engineering: A, 2014, 614: 193−198.

[53] ZHU Jia-lin, DENG Chao, LIU Ya-hui, LIN Nan, LIU Shi-feng. Effects of annealing temperature on recrystallization texture and microstructure uniformity of high purity tantalum [J]. Metals, 2019, 9(1): 75.

DS 轧制弱化超高纯钽厚度方向的织构梯度

于 凯[1]，徐龙飞[1]，王 丽[1,2]，李桂鹏[3]，Xiao-dan ZHANG[4]，王玉辉[1]

1. 燕山大学 国家冷轧板带装备及工艺工程技术研究中心，秦皇岛 066004；
2. 重庆工业职业技术学院 机械工程学院，重庆 401020；
3. 同创(丽水)特种材料有限公司，丽水 323000；
4. Department of Civil and Mechanical Engineering, Technical University of Denmark, DK-2800 Kgs. Lyngby, Denmark

摘 要：传统的同步轧制工艺往往会产生贯穿板材厚度方向的显微组织和织构梯度。本研究以超高纯度 (99.999%，质量分数) 钽为原材料，采用可动态偏移和调整剪切力的轧制(DS 轧制)工艺解决超高纯钽板的织构梯度问题，利用 Deform 3D 软件分析了超高纯钽板在 DS 轧制和同步轧制过程中的应变和应力分布，并且利用电子背散射衍射对材料厚度方向的织构和显微组织进行了表征。结果表明，DS 轧制将平均切应变从 0.05 提高到 0.56，有效地解决了超高纯钽板的织构梯度问题，且切应力显著降低了{100}和{111}晶粒的储能取向依赖性。此外，DS 轧制可有效细化超高纯钽板再结晶晶粒，其平均晶粒尺寸减小了 30.9%。

关键词：钽；织构梯度；轧制；储存能；切应力

(Edited by Wei-ping CHEN)